Numerical investigation of the spiral solar air heater performance

S. A. Gandjalikhan Nassab

Mechanical Engineering Department, Shahid Bahonar University of Kerman, Kerman, Iran

Email: Ganj110@uk.ac.ir

Abstract: This paper presents a new design of a spiral solar air heater with a 90^0 turning of the air inside the passageway assembled between the absorber and bottom plate for the purposes of mixing process and extending surface of heat transfer that finally leads to higher performance. To enhance the thermal efficiency, an air gap is considered at the top of the solar collector to reduce heat loss. The proposed solar collector is simulated numerically by the Finite Element Method using the COMSOL software. The set of governing equations for both forced and free convection turbulent air flows are solved based on the RNG k–ε turbulence model. In the energy equation solution, the effect of surface-to-surface radiation as an important phenomenon in solar collectors is considered. Numerical results reveal a high thermal efficiency of 75% for the test case with 100 W/m^2 solar heat flux and air mass flow rate of 0.01 kg/s. Compared to the conventional smooth duct solar air heater with 35% thermal efficiency, the designed solar collector operates with a higher performance, and a more than 100% increase in thermal efficiency is achieved due to the applied technique with the limitation of pressure drop which is increases about three times in spiral solar air heater.

Keywords: Spiral solar air heater, finite element method, efficiency, Turbulent convection flow, solar energy system

Nomenclature

A	Area ($\boldsymbol{m^2}$)	τ_g	Glass transmissivity
a	Air gap thickness (m)	β	Volumetric thermal expansion (1/K)
b	Height of the passageway (m)	μ	Fluid Viscosity (Pa.s)
$\boldsymbol{C_p}$	Gas specific heat (kJ/kg K)	ρ	Fluid density (kg/m^3)
h	Convection coefficient (W/m^{2}K)	υ	Dynamic viscosity (m^2/s)
k	Thermal conductivity (Wm^{-1}K^{-1})	κ	Turbulent kinetic energy (m^2/s^2)
L	Length of heater (mm)	ϵ	Turbulent dissipation (m^2/s^3)
$\dot{m}$	Mass flow rate (kg/s)	δ	Thickness (m)
p	Pressure (Pa)	**Subscript**	
q	Heat flux (W/m^2)	*abs*	Absorber
Ra	Rayleigh number	*amb*	Ambient
		i, j	Indices
Re	Reynolds number =$\rho\overline{V_{in}}D_h/\mu$	*bp*	Bottom plate
T	Temperature (K)	*g*	Glass
$\boldsymbol{U_i}$	Velocity component (m/s)	*in*	Inlet
(x, y)	Coordinates (m)	*ins*	Insulation
Greek symbols		*out*	Outlet
α_g	Glass absorptivity	*t*	Turbulence
ρ_g	Glass reflectivity		

1. Introduction

Radiative solar energy is both clean and abundant, with a wide distribution and many uses. One of the well-known solar energy systems is the simple structure solar air heater (SAH), in which the solar irradiation converts into air enthalpy to provide high-temperature airflow for use in many applications such as dehumidification, drying of agricultural products, energy storage, and space heating. The main advantages of this solar collector are the low cost and easy maintenance, but the heat convection coefficient between the flowing air and heated surface is low which leads to a low performance. There are a huge number of numerical and experimental studies for convection enhancement. A review of various techniques for increasing the efficiency of SAHs was given by Ahirwar and Kumar [1]. That study concentrated on four methods including artificial roughness and ribs on the absorber plate, jet impingement, piezo-electric fan, and phase change material. It was revealed that the maximum thermal hydraulic performance factor for noncircular ribs, ribs with a rectangular cross-section, ribs with an equilateral cross-section, and jet impingement are

equal to 1.44, 1.29, 2.11, and 3.66, respectively. Most of the suggested methods published in the literature deal with convection augmentation by increasing the surface and coefficient of heat transfer by employing fins [2], artificially roughened surfaces [3], vortex generators [4], porous segments [5], Wavy channels [6], perforated absorber plates with different geometries [7], jet impingement method [8], converged shape of air duct [9, 10] and using radiating working gases [11].

Recently, the author proposed a circular SAH in which the rotating air flow which has a vortex pattern inside the air vessel of the heater takes place due to entering the inlet flow in a tangential direction from the inlet tube attached to the side wall [12]. Both numerical and experimental results revealed about a 100% increase in thermal efficiency compared to the conventional plane SAHs. Some studies have shown that the presence of a spoiler inside SAH enhances the convection heat transfer and leads to an increase in thermal efficiency [13, 14]. In the numerical and experimental study by Li [15], a dual-spoiler SAH was presented and examined by a combination of a dual air duct with a serpentine passageway. It was revealed that the thermal efficiency increases by 21.74% compared with the conventional SAH.

Currently, the channels of SAH are designed with a serpentine passageway composed of spoilers. The obtained findings showed that serpentine SAH could improve the performance of solar collectors, but at the same time, a distinct recirculated vortex flow was formed at the end of baffle, where the convection airflow deflects 180°. This process causes a high-temperature recirculated zone and leads to a low convection coefficient. To remove this inability, a spiral solar air heater (SSAH) is proposed and examined experimentally in a paper by Jia et al. [16], in which there is only a 90° turning of the channel. The designed solar heater contains the insulation layer at the bottom, and the glass cover at the top, under which an absorber plate with spiral air passages is installed. In that experimental work, it was reported that compared with the conventional SAH, the ultimate thermal performance of SSAH is improved and up to 65% thermal efficiency was assessed.

The effect of the number of longitudinal side walls on flow and heat transfer behaviors of a spiral SAH was analyzed and examined numerically by Jia et al. [17]. In accordance with the analysis of the effective efficiency and economic benefits, the spiral SAH with two longitudinal side walls was distinguished as the optimum structure. Also, the correlations of Nusselt number and pressure drop of solar collector were found by applying the least equate method.

Four different types of spiral flow air collectors were examined numerically by Jia et al. [18]. The aim was to evaluate the effect of the baffle structure on the microscopic characteristics of the airflow and convection heat transfer. It was revealed that the solar collector with two deflectors has the optimum structure and maximum efficiency.

A new design of a SAH with a spiral airflow path was studied both numerically and experimentally by Amara et al. [19]. In simulations, the ANSYS FLUENT software was employed using the SST turbulent model. Different baffle heights under different air mass flow rates were tested numerically and the maximum thermal efficiency of 59% was obtained for the optimum design.

As a continuation of the study in Ref. [16], and to obtain a higher performance, the present work aims to design and examine an SSAH with a lower rate of heat loss and increased thermal efficiency. The installed baffles between the absorber and bottom plate which have formed as a unit element provide a spiral form for the air passageway from the inlet to the outlet section inside the solar collector. It is expected that a large amount of thermal energy is transferred into the convective air flow at each passage by the heated surfaces from the above, below, and the lateral sides by the absorber, bottom plate, and the installed baffles, respectively. This configuration was not applied in the SSAH in Ref. [16], such that the heated surfaces only consist of the absorber plate with the installed baffles. Also, in the present solar collector, a lower rate of heat loss takes place via the glass cover due to the considered air gap at the top of the collector, which was not applied in Ref. [16]. In the numerical simulation, the momentum and energy equations for the free convection airflow at the top of the collector and the forced convection airflow through the spiral air passageway along with the conduction equation for the solid parts are solved simultaneously by the finite element method (FEM). The obtained numerical data is depicted in terms of isotherm plots and velocity and pressure distributions in different parts of the designed SSAH.

2. Computational model

Figs. 1 and 2 illustrate the schematics of the analyzed SSAH. The present solar collector consists of a glass cover, air gap, and absorber plate integrated with the bottom plate. The geometrical dimensions with the values of some thermo-physical properties are tabulated in Tables. 1 and 2. Airflow with the ambient temperature and fully developed velocity profile enters the heater with $\dot{m} = 0.01$ kg/s. The value of Reynolds number defined as $Re = \rho \overline{V_{in}} D_h / \mu$ becomes equal to 7500 corresponds to the turbulent forced convection flow ,and for the natural convection flow inside the

air gap with the height of a=2 cm, the value of Rayleigh number based on the temperature difference $\Delta T = q_{sun}.a/k$ by the definition of $Ra = g\beta\Delta T a^3/\upsilon\alpha$ is greater than $Ra_c = 5 \times 10^4$ denotes the turbulent regime [20].

Table 1: Material properties [13]

Physical properties	Absorber	Insulation	Baffles	Bottom plate	Glass cover
Conductivity [W/m.K]	400	0.036	400	400	0.8
Surface emissivity	0.97	_	0.97	0.97	0.97
Reflectivity	0.03	_	0.03	0.03	0.02
Transmissivity	0	0	0	0	0.95

Table. 2: Values of the geometrical parameters

Parameter	a	b	δ_{baffle}	δ_g	δ_{abs}	δ_{bp}	δ_{ins}
Value (mm)	20	50	4	4	4	4	50

To evaluate the performance of a solar collector, the thermal efficiency, η_t, and thermohydraulic efficiency, η_{thyd} , should be calculated via the following relations [7, 12]:

$$\eta_t = \frac{\dot{m}c_p(T_{mout} - T_{in})}{q_{sun}.A} \quad (1)$$

$$\eta_{thyd} = \frac{\dot{m}c_p(T_{mout} - T_{in}) - C(\frac{\dot{m}\Delta p}{\rho})}{q_{sun}.A} \quad (2)$$

Based on Eq. 2, the pumping power, $\frac{\dot{m}\Delta p}{\rho}$, is considered when calculating the thermohydraulic efficiency. In this equation, parameter C is the factor due to the conversion of thermal energy to mechanical energy, and it is equal to 5.56. [7, 12].

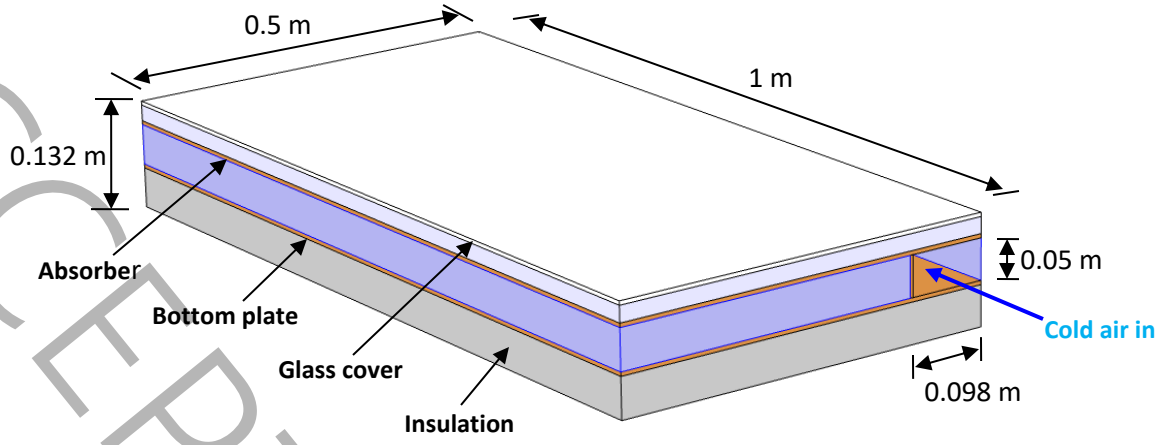

a) Upper view

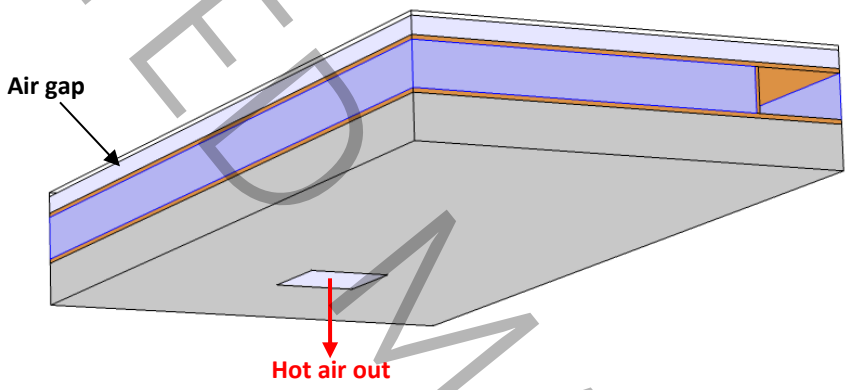

b) Lower view

Fig. 1: Schematic of the SAH

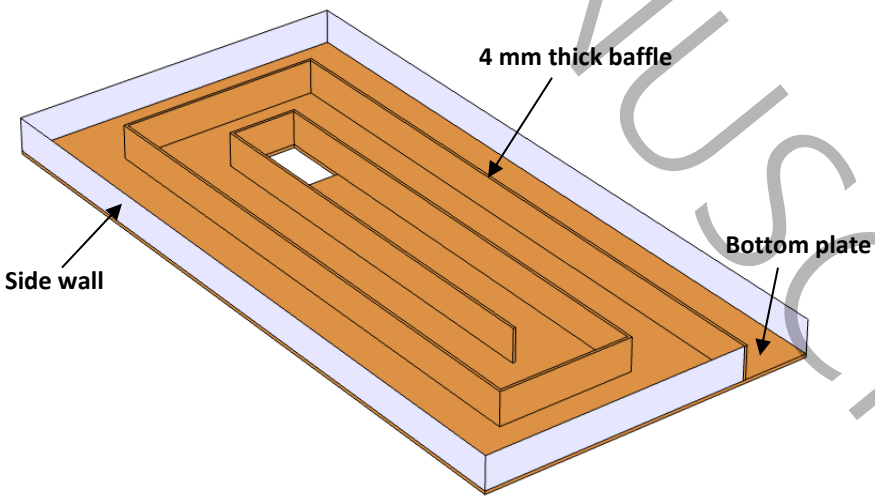

Fig. 2: Bottom plate including the air passageway

2.1 Governing equations

The tensor notation of the RANS forms of the governing equations with the quasi-steady, incompressible, and three-dimensional turbulent flow, and the conduction equation for the solid parts can be written as follows:

a) Forced convection inside the air passages

$$\frac{\partial u_i}{\partial x_i} = 0 \tag{3}$$

$$u_j \frac{\partial u_i}{\partial x_j} = \frac{1}{\rho}\frac{\partial p}{\partial x_i} + \frac{1}{\rho}\frac{\partial}{\partial x_j}[(\mu + \mu_t)(\frac{\partial u_i}{\partial x_j} + \frac{\partial u_i}{\partial x_j})] \tag{4}$$

$$u_j \frac{\partial T}{\partial x_j} = \frac{\partial}{\partial x_j}[(\frac{\mu}{\mathrm{Pr}} + \frac{\mu_t}{\mathrm{Pr}_t})]\frac{\partial T}{\partial x_j} \tag{5}$$

b) Free convection inside the air gap

$$\frac{\partial u_i}{\partial x_i} = 0 \tag{6}$$

$$u_j \frac{\partial u_i}{\partial x_j} = \frac{1}{\rho}\frac{\partial p}{\partial x_i} + \frac{1}{\rho}\frac{\partial}{\partial x_j}[(\mu + \mu_t)(\frac{\partial u_i}{\partial x_j} + \frac{\partial u_i}{\partial x_j})] + S \tag{7}$$

$$u_j \frac{\partial T}{\partial x_j} = \frac{\partial}{\partial x_j}[(\frac{\mu}{\mathrm{Pr}} + \frac{\mu_t}{\mathrm{Pr}_t})]\frac{\partial T}{\partial x_j} \tag{8}$$

Where the source term, $S = \rho g[1 - \beta(T - T_{ref})]$, is considered only for the momentum equation in the z-direction due to the buoyancy effect

c) Conduction equation for solid parts

$$\frac{\partial}{\partial x_j}(\frac{\partial T}{\partial x_j}) + \frac{q_{Sun}.\alpha_g}{k_g.\delta_g} = 0 \tag{9}$$

The second term in the LHS is considered only for the glass cover due to its radiative absorption across this element.

It should be mentioned that based on the assumption of the quasi-steady condition, the thermal storage inside the solar collector is ignored. This condition can be employed if there are not any

sudden changes in the climate condition such as in the value of incident solar radiation and ambient temperature.

Based on the applied κ-ε turbulence model in the present RANS problem for the analysis of convection flows, the turbulent kinetic energy and its dissipation rate are computed by the following equations [21].

$$\rho u_i \frac{\partial \kappa}{\partial x_i} = \frac{\partial}{\partial x_j}[(\mu + \frac{\mu_t}{\sigma_k})\frac{\partial \kappa}{\partial x_j}] + G_\kappa - \rho\varepsilon \quad (10)$$

$$\rho u_i \frac{\partial \varepsilon}{\partial x_i} = \frac{\partial}{\partial x_j}[(\mu + \frac{\mu_t}{\sigma_\varepsilon})\frac{\partial \varepsilon}{\partial x_j}] + C_{\varepsilon 1}\frac{\varepsilon}{\kappa}G_\kappa - C_{\varepsilon 2}\rho\frac{\varepsilon^2}{\kappa} \quad (11)$$

It should be mentioned that the choice of the applied κ-ε turbulence model is based on the previous study by the author in which the numerical results by four well-known turbulence models were compared and investigated for having more reliable results in the analysis of rotating airflow which is almost similar to that happens in Ref. [12]. More details about the governing equations and the applied turbulence model also the values of constants in these equations are reported in Ref.s [12, 21].

2.2 Boundary conditions

For velocity computation, the no-slip boundary condition is employed on the solid-fluid interfaces. Fully developed cold air flow enters with ambient temperature and the imposed mass flow rate. Also, the pressure outlet is applied at the exit section. At the upper surface of the glass cover and lower surface of the insulation, the convection boundary condition with $h_{eq} = h_{conv} + h_{rad}$, was considered. The radiative and convective parts of the equivalent convection coefficient are computed as [12]:

$$h_{rad} = \sigma\varepsilon_g(\frac{T_g^4 - T_{sky}^4)}{T_g - T_{amb}}) \quad (12)$$

$$h_{conv} = 5.7 + 3.8V_{wind} \quad (13)$$

Where the sky temperature can be calculated with the following relation:

$$T_{sky} = 0.0552\, T_{amb}^{1.5} \tag{14}$$

Also, a uniform heat flux of $\tau_g \times \alpha_{abs} \times q_{sun}$ is considered on the upper surface of the absorber plate due to the absorbed solar irradiation.

2.3 Grid study

To find an optimum grid size and the mesh-independent numerical solution, five different meshes were tested. The grid generation was done by clustering near the interfaces and in the regions with high gradients and also considering smaller mesh sizes inside the velocity boundary layers. The air outlet temperature for each case was obtained and the variation of this parameter with the number of elements is plotted in Fig. 3 the optimum grid with 280000 tetrahedra elements under which the percentage of temperature change becomes less than 1% is chosen and used in all subsequent simulations. During the iterative numerical procedure based on the FEM for solving the set of governing equations, the converged solution for each of the dependent variables was assumed to be achieved while the amount of residual in each of the equations including the conservations of mass, momentum, and energy and also the k- and ε- equations become less than 1.2×10^{-4}, based on the convergence curve plotted in Fig. 4. Also, a schematic of the meshed domain with the optimum number of grids is illustrated in Fig. 5.

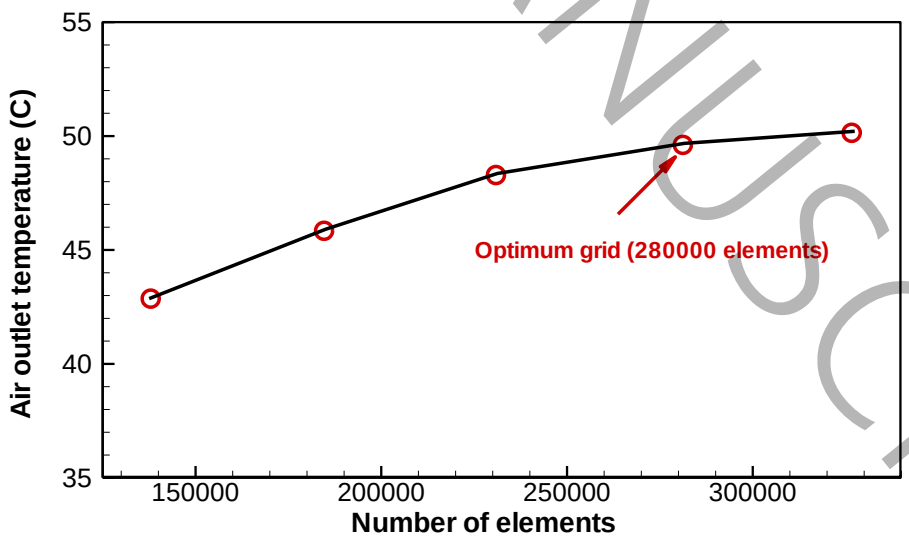

Fig. 3: Results of grid study for calculation of air outlet temperature

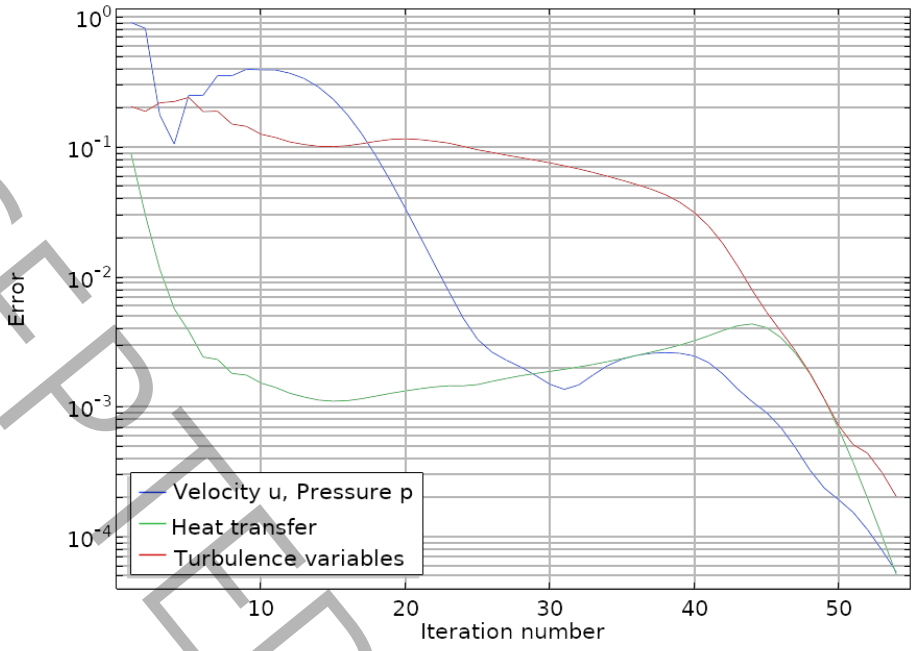

Fig. 4: Variations of the residuals during iterative steps

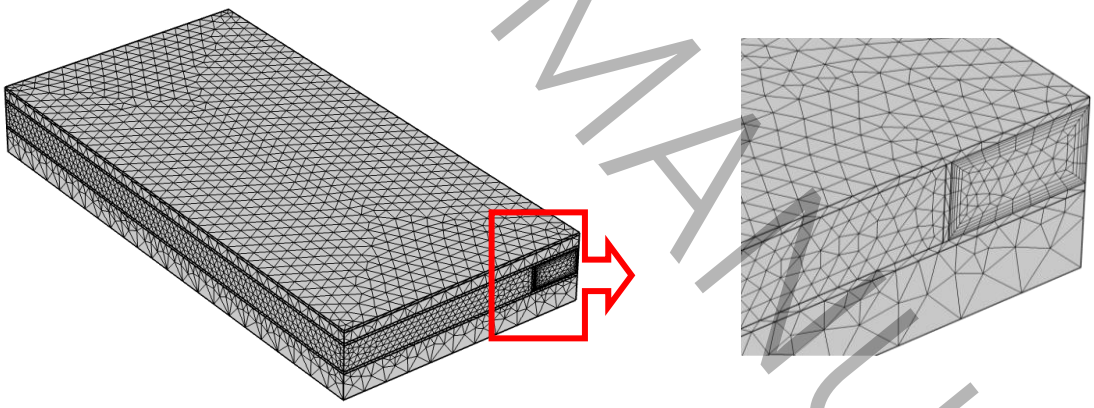

Fig. 5: Discretized computational domain

3. Validation

As noted in the introduction, the present designed SSAH is similar to the one studied experimentally by Jia et al. [16]. A photo of the test system examined in that work is shown in Fig. 6. In the present designed solar collector in addition to the elements used in the structure of solar collector studied in Ref. [16], an extra air gap is considered at the top for having a lower rate of heat loss and the configuration of the absorber, bottom plate, and the installed side walls provide a spiral shape for the air passageway as a compact unit. Therefore, by

eliminating the air gap and replacing the absorber plate with a glass cover in the present SSAH, the two solar collectors become the same. It is expected that with the present configuration, the extent of the heated surface which is in contact with the flowing air is increased which causes convection augmentation, in addition to the benefit of the spiral form of air passage. To validate the obtained results, the present findings from the numerical simulation of the studied SSAH in Ref. [16] are compared with the experimental data given in that reference. For this, the computed air temperature difference at different values of the solar irradiation are plotted in Fig. 7 and compared against the experiment. This figure shows that much more thermal energy is transferred into the airflow as the solar irradiation gets higher values. Comparison between the data presented in Fig. 7 shows a good consistency, such that the maximum percentage of error between the numerical and experimental results is about 7.5% that takes place at $q_{sun} = 650\ \mathrm{W/m^2}$. The difference between the results is due to the numerical and round of errors in the CFD method and also the measurement mistakes during experiment.

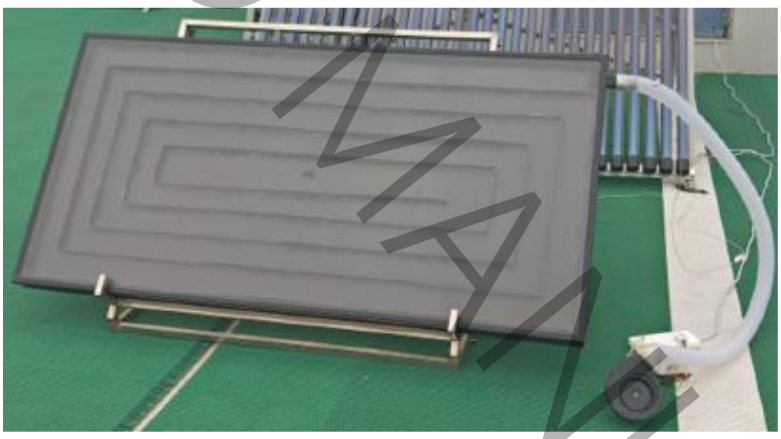

Fig. 6: Photo of the test system [16]

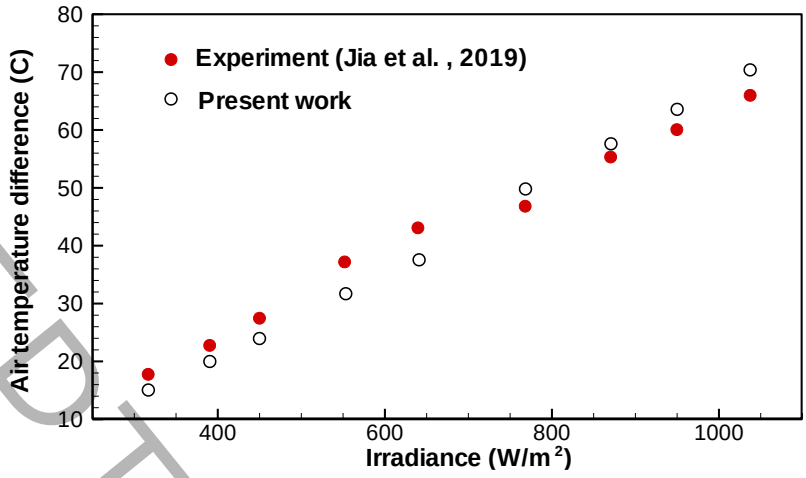

Fig. 7: Validation of the numerical results with experiment, $\dot{m} = 0.0146$ kg/s

4. Results

To assess the thermo-hydrodynamic characteristics of the designed SSAH and its ability to convert solar irradiation into air enthalpy, the numerical solution of the governing equations including the velocity, pressure, and temperature for both free and forced convection air flows inside the heater and the temperature distribution inside all solid elements is obtained. In all simulations, the air mass flow rate and the solar heat flux are kept constant equal to $\dot{m} = 0.01$ kg/s, $q_{sun} = 1000$ W/m^2, except in the calculations of Fig. 16, where the effects of these parameters are under study. The forced convection flow behavior is shown in Fig. 8 by plotting the contours of velocity magnitude inside the passageway of SSAH. The stagnant flows at the corners are seen with this fact that a slight increase in the velocity magnitude along the flow direction takes place due to a density decrease in the airflow toward the outlet section. The temperature distribution inside the whole part of solar collector is depicted in Fig. 9. As expected, the maximum temperature belongs to the absorber surface where a great part of the incoming solar radiation is absorbed. The surface radiation between the heated absorber and the bottom plate including the installed side walls also leads to a high temperature for the boundaries of the spiral air passage. The air gap at the top of collector decreases the glass cover temperature and then the rate of heat loss via this element.

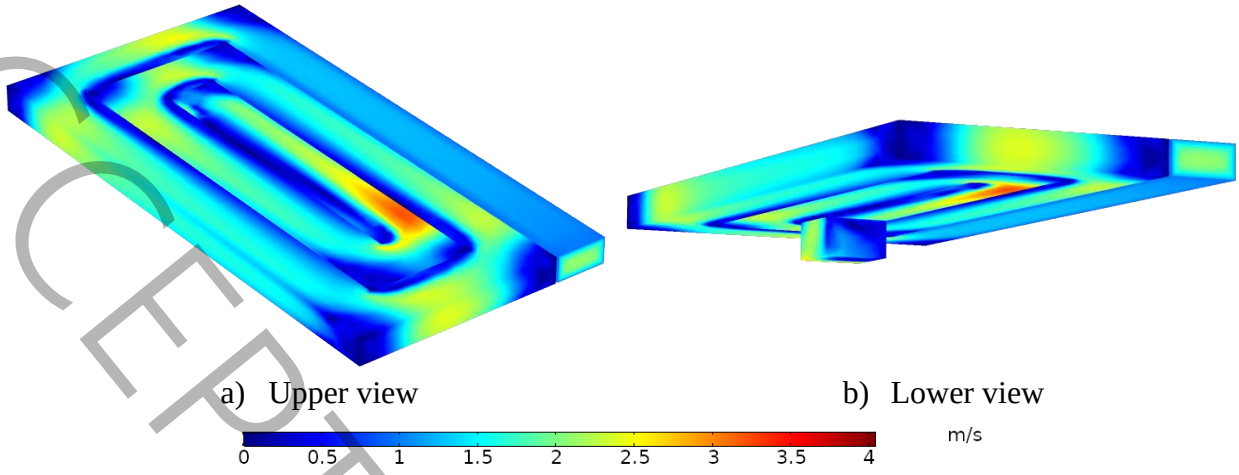

Fig. 8: Velocity magnitude contour plot

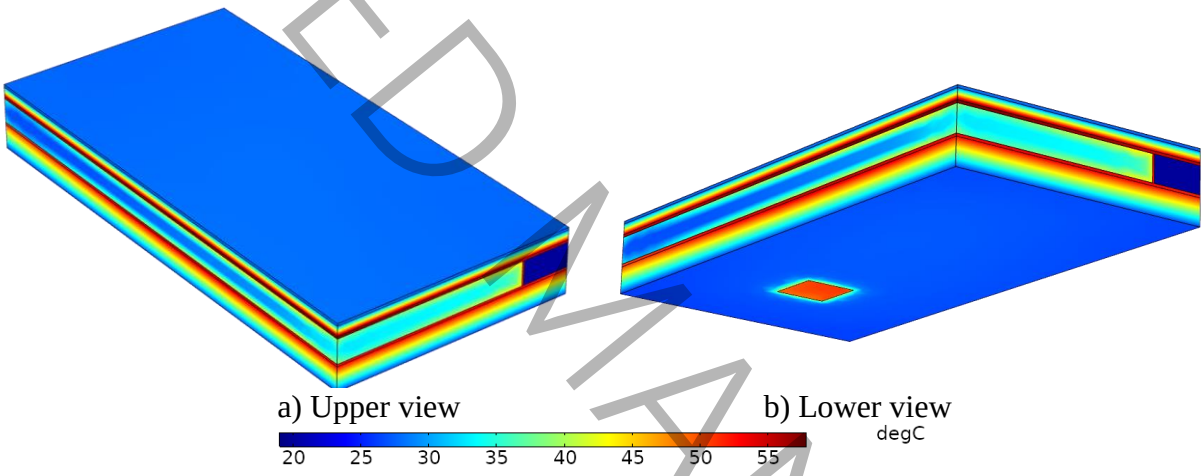

Fig. 9: Isotherm plots inside the SAH

Since, the inner region of the SSAH could not be seen in Fig. 8, an attempt is made in subsequent figures to show the temperature variations inside the inner parts. For this, the region of airflow is chosen in Fig. 10 and the isotherm plots are presented in this figure. As seen, a low-temperature zone takes place at the vicinity of the inlet section. At the interfaces with the absorber, bottom plate, and side walls of the passages, effective convection heat transfer takes place which leads to the air temperature increase along the flow direction up to the outlet section. From all of the air passages, the first pass is much more effective with the maximum air temperature increase. It should be noted that one of the main factors of convection enhancement in spiral heaters is the mixing process and breaking thermal boundary layer at the corners where the airflow turns 90^0.

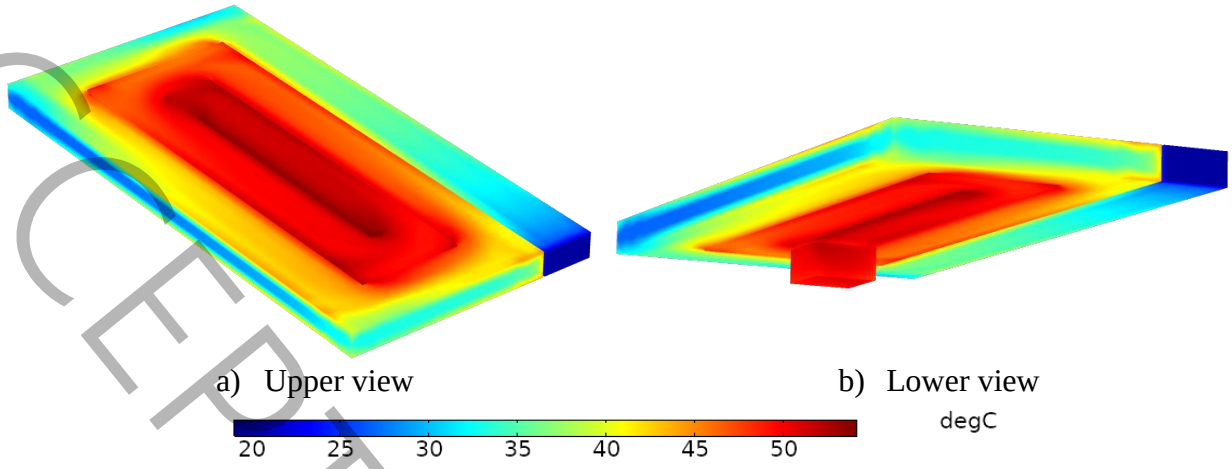

a) Upper view b) Lower view

Fig. 10: Isotherm plot inside the convection air flow

The absorber and bottom plate with their installed side walls for the passages are the main components of the SSAH. The surfaces of these elements are heated due to the absorbed solar heat flux and the internal surface radiation. As Fig. 11 shows, it is seen that these elements are not too hot due to the effective convection heat transfer with the flowing air. Also, there is a small temperature variation of less than 3 C on the absorber surface due to the high thermal conductivity of this element and the uniform absorbed incident radiation at the top. For the bottom plate including the air passages, the minimum temperature takes place close to the air inlet section where the cold air enters into the heater and the maximum temperature is near to the central region.

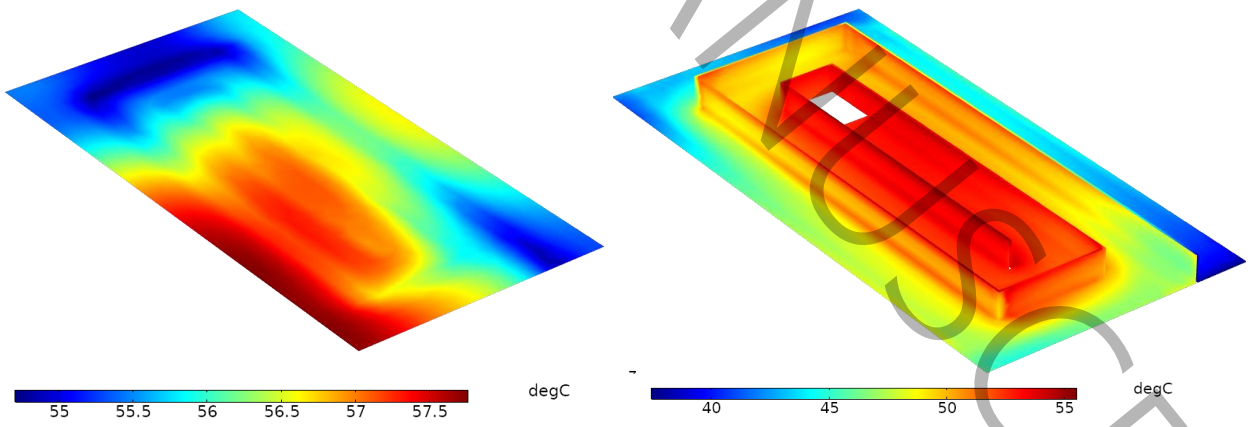

a) Absorber surface b) Bottom plate surface

Fig. 11: Temperature distribution over the absorber and bottom plate surfaces

The isotherm plots inside the insulation are depicted in Fig. 12. As seen, there is a large temperature gradient along the vertical z-direction with more than 25 C temperature difference across the 5 cm thickness, which is due to choosing well-insulated material for this element. Also, on each axial plane, almost a uniform temperature takes place.

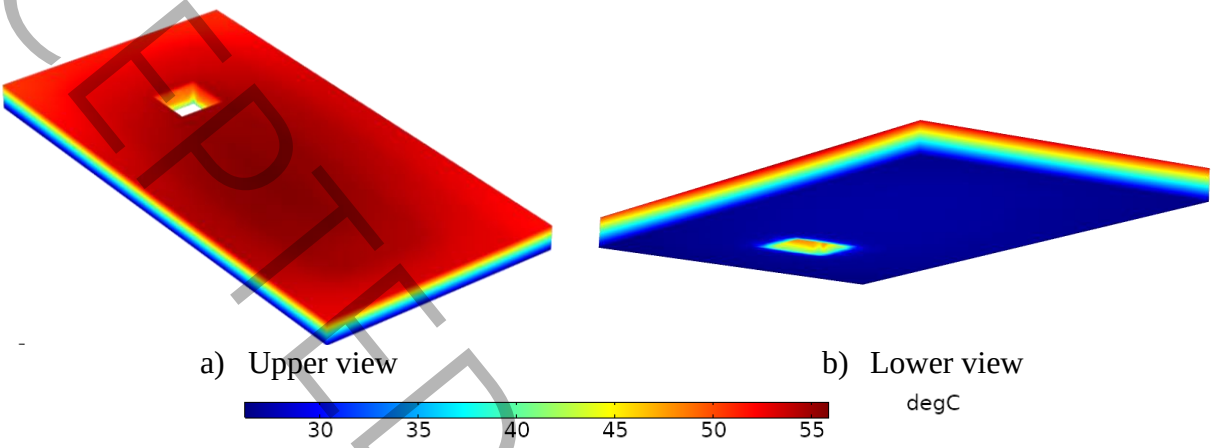

a) Upper view b) Lower view

Fig. 12: Isotherm plots inside the insulation layer

The temperature distributions on the boundary surfaces at the top and bottom of the SSAH, where the heat loss to the ambient takes place are presented in Fig. 13. As seen, the glass surface is in almost low temperature due to the effective role of air gap from below. This is a desired phenomenon that prevents a high rate of heat loss. If one compares the isotherms plotted in Fig. 13-a and b, it can be found that for the proposed SSAH, the main source of heat loss takes place via the insulation surface whose average temperature is about 3 C more than the glass cover.

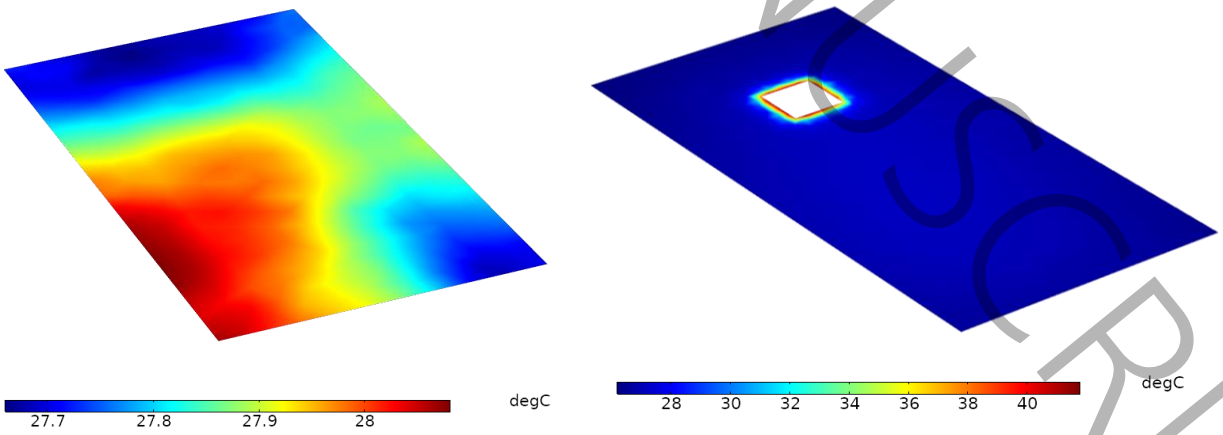

a) Glass surface b) Insulation surface

Fig. 13: Temperature distributions over the outer surfaces of the glass cover and insulation

To evaluate the values of convection coefficient along the flow passes, the Nusselt number defined as $Nu = hD_h/k$ is computed for each axial section perpendicular to the airflow direction from the inlet to the outlet section and its variation is plotted in Fig. 14. This figure reveals a decreasing trend of Nu along each of the flow passes due to growing the thermal boundary layer. Just after the 90 degrees change in flow direction at each of the corners, a slightly increase in convection coefficient is depicted in Fig. 14 which is due to flow mixing and breaking thermal boundary layer as airflow passes through these sections.

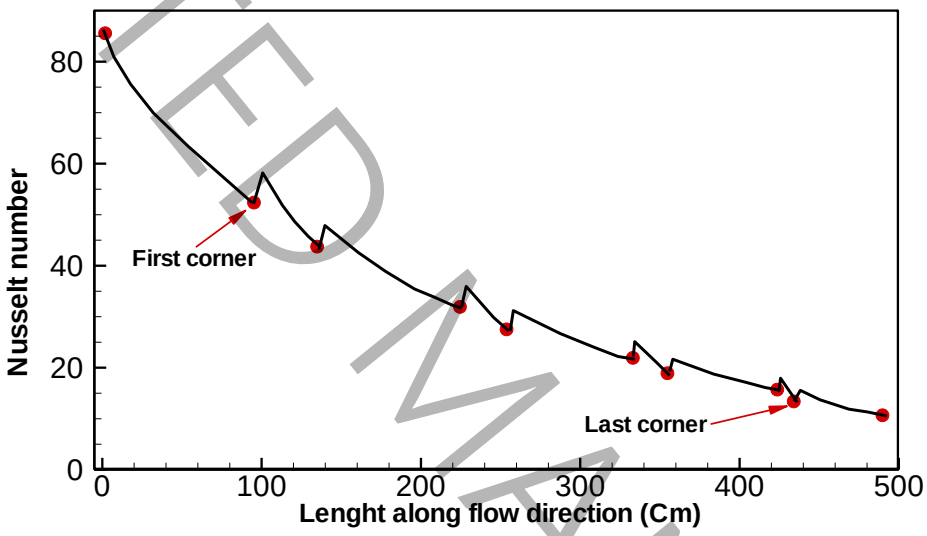

Fig. 14: Variation of Nusselt number along the flow direction from the inlet to the outlet section

Fig. 15 shows the air pressure field inside the SSAH by plotting the isobar contours. The air pressure drop along the flow direction at each of the air passages is clearly seen in this figure, such that the overall pressure drop from the inlet to the outlet section in the studied test case with $\dot{m} = 0.01$ kg/s is $\Delta p = 17$ Pa. In comparison to the conventional smooth duct SAH which is also simulated in the present work with a 5 Pa pressure drop, $\Delta p = 17$ Pa is relatively high. This behavior is due to the spiral form of the air passageway and the sudden change of flow direction at the corners.

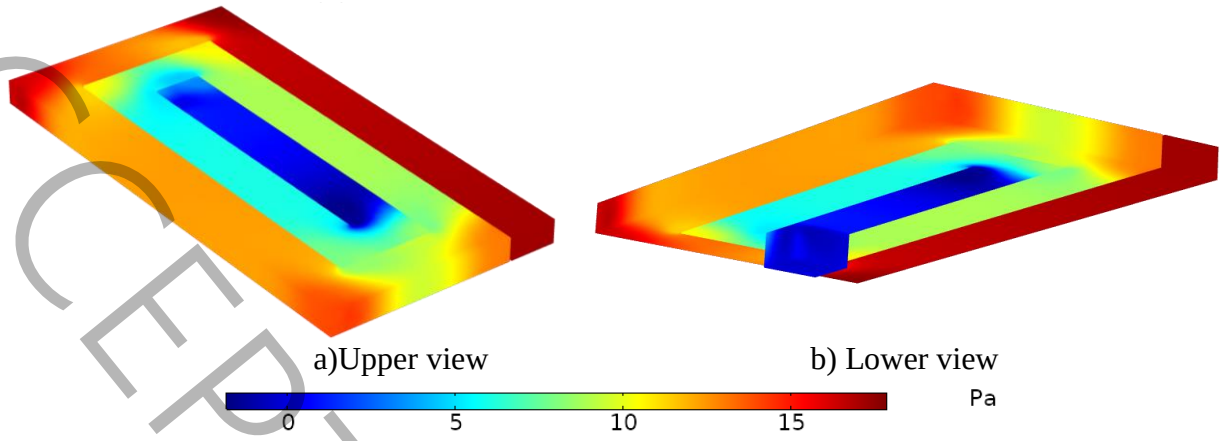

Fig. 15: Isobar contours for forced convection airflow

As the performance of SAH can be evaluated by the thermal efficiency defined in Eq. 1, the value of this parameter at three different air mass flow rates is calculated and shown in Fig. 16. Results reveal high thermal efficiencies for the proposed SSAH, even when the solar collector operates under a low air mass flow rate. Fig. 16 also shows a slight decrease in thermal efficiency as the incident solar irradiation gets higher values. As demonstrated, up to 83% thermal efficiency is calculated for the designed SSAH under the condition of $\dot{m} = 0.012$ kg/s, and $q_{sun} = 800$ W/m^2, which is interesting.

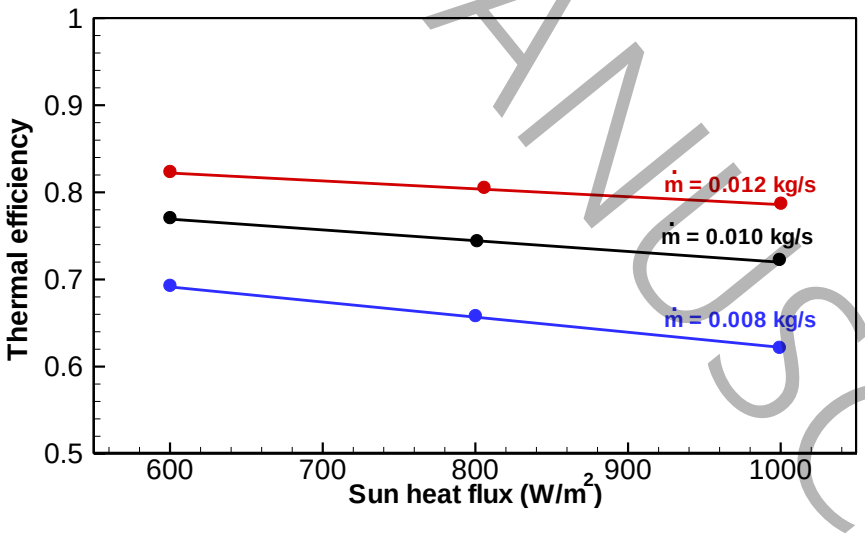

Fig. 16: Variation of the thermal efficiency with the sun irradiation

Finally, a comparative analysis is performed in this paper to compare the performance of the proposed solar collector with the convectional plane SAH. For this purpose, a plane SAH with a length of 1m and the width of 0.5 m and the same values of the geometrical parameters used in the

design of SSAH operating with $\dot{m} = 0.01\ \mathrm{kg/s}$, and $q_{sun} = 1000\ \mathrm{W/m^2}$ is simulated and the isotherm plots in the whole region of solar collector and for the convection airflow are plotted in Figs. 17-a and b. As seen, the absorber temperature is very high in comparison to the proposed SSAH. From the numerical findings, one can compute the absorber average temperature of 110 °C for the conventional type, while the value of this parameter for the designed SSAH is 57 °C. This behavior leads to a higher rate of heat loss and low efficiency. The main factor for this process is the low convection coefficient between the heated absorber and airflow in conventional solar collectors, and the thin heat penetration depth from the heated absorber into the convection flow shown in Fig. 17-b is due to this fact. A comparison is also made in Table. 3, in which the thermal efficiencies of these two analyzed solar collectors are tabulated at different air mass flow rates. Noticing the fact that there is an increasing trend for the thermal efficiency with the increase of air mass flow rate, a more than 100% efficiency increase is found for the designed SSAH compared with the conventional plane SAH.

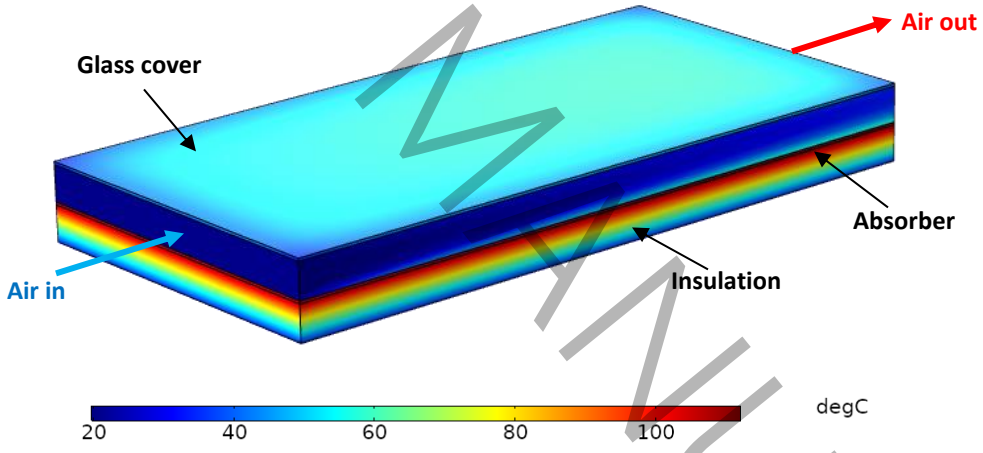

a) Isotherm plots inside the conventional plane SAH

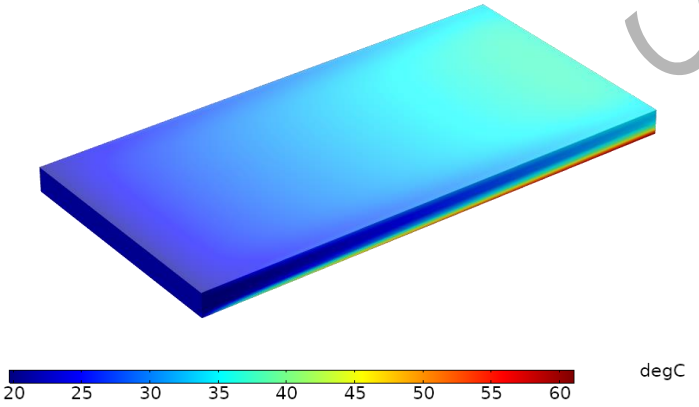

b) Isotherm plots inside the domain of airflow

Fig. 17: Thermal behavior of the conventional plane SAH

Table .3: Thermal efficiencies of conventional SAH and SSAH, $q_{sun} = 1000\ W/m^2$

$\dot{m}$	0.008 kg/s	0.01 kg/s	0.012 kg/s
$\eta_{t\,SAH}$	0.31	0.35	0.39
$\eta_{t\,SSAH}$	0.62	0.75	0.80

As it was noted in the description of Fig. 15, the designed SSAH has more pressure drop compared to the conventional smooth duct SAH which is due to the difference in the airflow patterns. To study this subject, the variations of pressure drop with the air mass flow rate are plotted for these two types of solar air heaters in Fig. 18. As expected, the pressure drop gets higher values with the increase of air mass flow rate such that the rate of pressure drop increase in SSAHs is much greater than the one for the conventional SAH. This behavior is due to the airflow pattern inside the spiral-shaped passages in SSAH.

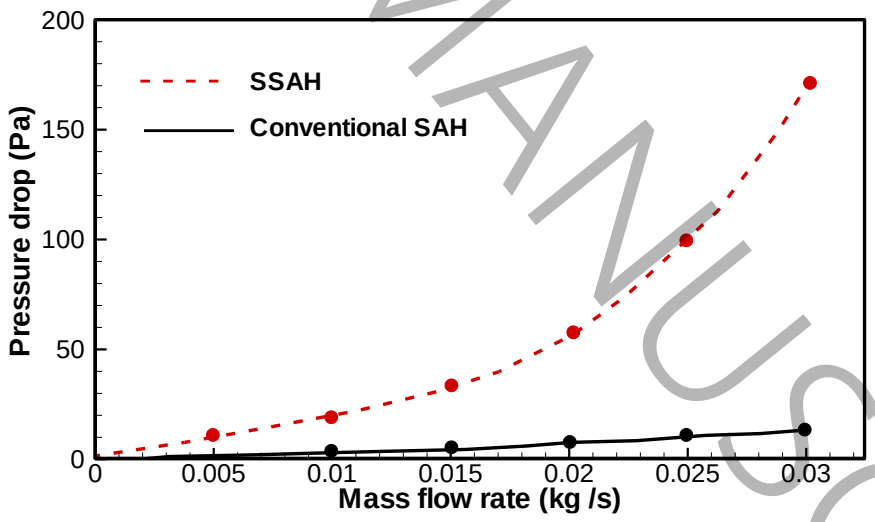

Fig. 18: Variation of pressure drop with the air mass flow rate

To evaluate the performance of solar collectors in converting sun heat flux into air enthalpy with considering the effect of pressure drop, the thermohydraulic efficiency should be calculated based on Eq. 2. The variations of both thermal and thermohydraulic efficiencies, η_t and η_{thyd} with air

mass flow rate for the SSAH and conventional smooth duct SAH are drawn in Fig. 19. It is seen that the SSAH is more efficient, such that its thermal and thermohydraulic efficiencies are about two times of the similar parameters for the conventional SAH. In the range of low air mass flow rates, Fig. 19 demonstrates increasing trends for the thermohydraulic efficiencies of both solar collectors, but due to the growth of pumping power, a decrease in η_{thyd} takes place for SSAH when it operates at high values of air mass flow rate, say $\dot{m} \geq 0.025$ kg/s.

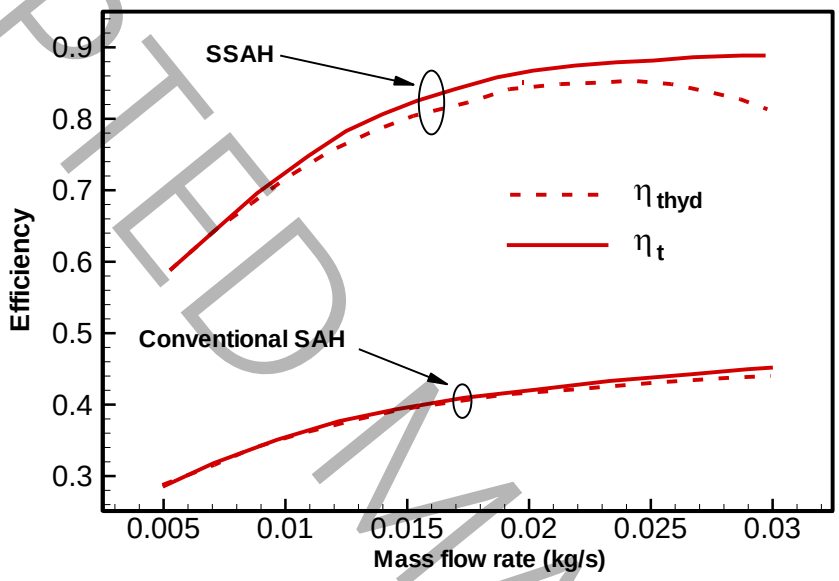

Fig 19: Variations of thermal and thermohydraulic efficiencies vs air mass flow rate, $q_{sun} = 1000\ \mathrm{W/m^2}$

5. Conclusion

This study was dedicated to examine the performance of a proposed SSAH with an air gap and a special configuration of the heated surfaces including the bottom plate, air passages, and absorber. By utilization of a CFD-based numerical analysis, the set of governing equations for steady 3-D turbulent forced and free convection airflows and the conduction equations for solid elements along with considering the surface-to-surface radiation has been solved by the finite element method. The main conclusion can be summarized as follows:

1- The applied designed form proved well its potential in heat transfer augmentation and high performance. Such that the breaking thermal boundary layer and mixing process through the 90-degree change in flow directions at the corners and the extending surface of heat

transfer by the design of spiral air passages between the heated bottom plate and absorber provide a considerable performance improvement.

2- The applied air gap at the top of the collector plays a major role in decreasing the glass cover temperature and leads to a much lower rate of heat loss.

3- The highest efficiency of 83% is calculated for the proposed SSAH under the condition of $\dot{m} = 0.012 \frac{kg}{s}$ and $q_{sun} = 1000 \frac{W}{m^2}$ that shows a 100% increase in thermal efficiency compared with the conventional smooth duct SAHs.

References

[1] B. kumar Ahirwar, Review on different techniques used to enhance the thermal performance of solar air heater, International Journal of Heat and Mass Transfer, 220 (2024) 124979.

[2] O. Manca, S. Nardini, D. Ricci, Numerical study of air forced convection in a rectangular channel provided with ribs, in: International Heat Transfer Conference, 2010, pp. 861-870.

[3] S. Singh, S. Chander, J. Saini, Heat transfer and friction factor correlations of solar air heater ducts artificially roughened with discrete V-down ribs, Energy, 36(8) (2011) 5053-5064.

[4] Y. Sheikhnejad, S.A.G. Nassab, Enhancement of solar chimney performance by passive vortex generator, Renewable Energy, 169 (2021) 437-450.

[5] P. Naphon, Effect of porous media on the performance of the double-pass flat plate solar air heater, International communications in heat and mass transfer, 32(1-2) (2005) 140-150.

[6] S. Singh, Utilising fractional porous interface for high thermal performance of serpentine wavy channel solar air heater, Applied Thermal Engineering, 205 (2022) 118044.

[7] S.P. Shetty, N. Madhwesh, K.V. Karanth, Numerical analysis of a solar air heater with circular perforated absorber plate, Solar Energy, 215 (2021) 416-433.

[8] O.R. Alomar, H.M. Abd, M.M.M. Salih, Efficiency enhancement of solar air heater collector by modifying jet impingement with v-corrugated absorber plate, Journal of Energy Storage, 55 (2022) 105535.

[9] S. Gandjalikhan Nassab, Efficient design of converged ducts in solar air heaters for higher performance, Heat and Mass Transfer, 59(3) (2023) 363-375.

[10] S. Gandjalikhan Nassab, Three-dimensional CFD analysis of solar air heaters for improving thermal performance using converged air ducts, International Journal of Green Energy, 21(1) (2024) 43-53.

[11] M. Foruzan Nia, S.A. Gandjalikhan Nassab, A.B. Ansari, Numerical simulation of flow and thermal behavior of radiating gas flow in plane solar heaters, Journal of Thermal Science and Engineering Applications, 12(3) (2020) 031008.

[12] M.M. Addini, S.G. Nassab, Utilization of vortex flow pattern in the design of an efficient solar air heater, Solar Energy, 276 (2024) 112683.

[13] K. Matrawy, Theoretical analysis for an air heater with a box-type absorber, Solar energy, 63(3) (1998) 191-198.

[14] N. Moummi, S. Youcef-Ali, A. Moummi, J. Desmons, Energy analysis of a solar air collector with rows of fins, Renewable energy, 29(13) (2004) 2053-2064.

[15] X. Li, Design and Test of a Serpentine Double Channel Flat Plate Solar Air Heater, Bayi Agricultural University, (2017).

[16] B. Jia, F. Liu, D. Wang, Experimental study on the performance of spiral solar air heater, Solar Energy, 182 (2019) 16-21.

[17] B. Jia, F. Liu, X. Li, A. Qu, Q. Cai, Influence on thermal performance of spiral solar air heater with longitudinal baffles, Solar Energy, 225 (2021) 969-977.
[18] B. Jia, L. Yang, L. Zhang, B. Liu, F. Liu, X. Li, Optimizing structure of baffles on thermal performance of spiral solar air heaters, Solar Energy, 224 (2021) 757-764.
[19] W.B. Amara, A. Bouabidi, Experimental studies and 3D simulations for the investigation of thermal performances of a solar air heater with different spiral-shaped baffles heights, Journal of Building Engineering, 65 (2023) 105662.
[20] D.P.D. Fran P. Incropera, Introduction To Heat Transfer, 4 ed., Wiley, 2001.
[21] M. Tabatabaian, CFD Module: Turbulent Flow Modeling, Mercury Learning and Information, 2015.